

Light Field Super-Resolution Via Graph-Based Regularization

Mattia Rossi and Pascal Frossard

École Polytechnique Fédérale de Lausanne

mattia.rossi@epfl.ch, pascal.frossard@epfl.ch

Abstract—Light field cameras can capture the 3D information in a scene with a single shot. This special feature makes light field cameras very appealing for a variety of applications: from the popular post-capture refocus, to depth estimation and image-based rendering. However, light field cameras suffer by design from strong limitations in their spatial resolution, which should therefore be augmented by computational methods. On the one hand, off-the-shelf single-frame and multi-frame super-resolution algorithms are not ideal for light field data, as they do not consider its particular structure. On the other hand, the few super-resolution algorithms explicitly tailored for light field data exhibit significant limitations, such as the need to estimate an explicit disparity map at each view. In this work we propose a new light field super-resolution algorithm meant to address these limitations. We adopt a multi-frame alike super-resolution approach, where the complementary information in the different light field views is used to augment the spatial resolution of the whole light field. We show that coupling the multi-frame approach with a graph regularizer, that enforces the light field structure via non local self similarities, permits to avoid the costly and challenging disparity estimation step for all the views. Extensive experiments show that the proposed algorithm compares favorably to the other state-of-the-art methods for light field super-resolution, both in terms of PSNR and in terms of visual quality. Moreover, differently from the other light field super-resolution methods, the new algorithm provides reconstructed light field views with uniform quality, which happens to be an important feature for any light field application.

I. INTRODUCTION

We live in a 3D world but the pictures taken with traditional cameras can capture just 2D projections of this reality. The *light field* is a model that has been originally introduced in the context of image-based rendering with the purpose of capturing richer information in a 3D scene [1] [2]. This could be used in many applications, from post-capture refocusing to depth estimation or virtual reality. The light emitted by the scene is modeled in terms of rays, each one characterized by a direction and a radiance value. The light field function provides, at each point in space, the radiance from a given direction. The rich information captured by the light field function permits the rendering of arbitrary views in the 3D scene.

However, the light field is a theoretical model: in practice the light field function has to be properly sampled, which is a challenging task. A straightforward but hardware-intensive approach relies on camera arrays [3]. In this setup, each camera records an image of the same scene from a particular position and the light field takes the form of an array of views. More recently, the development of the first commercial

light field cameras [4] [5] has made light field sampling more accessible. In light field cameras, a micro lens array placed between the main lens and the sensor permits to virtually partition the main lens into sub-apertures, whose images are recorded altogether in a single shot [6] [7]. As a consequence, a light field camera behaves as a compact camera array, providing multiple simultaneous images of a 3D scene from slightly different points of view.

Even if light field cameras become very appealing, they still face the so called *spatio-angular resolution tradeoff*. Since the whole array of views is captured by a single sensor, a dense sampling of the light field in the angular domain (i.e., a large number of views) necessarily translates into a sparse sampling in the spatial domain (i.e., low resolution views) and vice versa. A dense angular sampling is at the basis of any light field application, as the 3D information provided by the light field data comes from the availability of different views. It follows that the angular sampling cannot be excessively penalized to favor spatial resolution. Moreover, even in the limit scenario of a light field with just two views, the spatial resolution of each one may be reduced to half of the sensor [6], which still happens to be a dramatic drop in the resolution. Consequently, the images rendered from light field data exhibit a significantly lower resolution than those from traditional cameras, and many light field applications, such as depth estimation, happen to be very challenging due to the low spatial resolution. The design of spatial super-resolution techniques, aiming at increasing the view resolution, is therefore crucial in order to fully exploit the potential of light field cameras.

The resolution may be improved by common single-frame super-resolution algorithms, and multi-frame ones. However, the light field data has a particular geometrical structure: on one side, it can be exploited for reconstruction, but on the other side it needs to be carefully preserved, as it encodes the scene geometry. A few super-resolution algorithms that are specifically tailored for light field data have been recently proposed in the literature too [8] [9] [10]. However, these algorithms are characterized by one or more undesirable features: the need to estimate the scene depth at each view before the super-resolution step, the need to apply the algorithm at each view independently in order to super-resolve the whole light field, and the use of learning-based procedures, which typically calls for a new training for each super-resolution factor and ties the quality of the final light field to the chosen training set.

In this work, we propose a new light field super-resolution

algorithm that overcomes these issues and provides a global solution that augments the resolution of all the views together, without an explicit a priori depth estimation step. In particular, we propose to cast the light field spatial super-resolution problem into a global optimization problem, whose objective function is designed to capture the relations between the light field views. The objective function comprises three terms. The first one enforces data fidelity, by constraining each high resolution view to be consistent with its low resolution counterpart. The second one is a warping term, which gathers for each view the complementary information encoded in the other ones. The third one is a graph-based prior, which regularizes the high resolution views by enforcing smoothness along the light field epipolar lines that define the light field structure. These terms altogether form a quadratic objective function that we solve iteratively with the proximal point method. The results show that our algorithm compares favorably to state-of-the-art light field super-resolution algorithms, both visually and in terms of reconstruction error.

The article is organized as follows. Section II presents an overview of the related literature. Section III formalizes the light field structure. Section IV presents our problem formulation and carefully analyzes each of its terms. Section V provides a detailed description of our super-resolution algorithm. Section VI is dedicated to the experiments that we carried out. Finally, section VII concludes the article.

II. RELATED WORK

The super-resolution literature is quite vast, but it can be divided mainly into two areas: single-frame and multi-frame super-resolution methods. In single-frame super-resolution, just one image from a scene is provided, and its resolution needs to be increased. This goal is typically achieved by learning a mapping from the low resolution data to the high resolution one, either on an external training set [11] [12] or on the image itself [13] [14]. Single-frame algorithms can be applied to each light field view separately in order to augment the resolution of the whole light field, but this approach would neither exploit the high correlation among the views, nor enforce the consistency between them.

In the multi-frame scenario, multiple images of the same scene are used to increase the resolution of a target image. To this purpose, all the available images are typically modeled as translated and rotated versions of the target one [15] [16]. The multi-frame super-resolution scenario appears to be close to the light field one, but the traditional global image warping model does not fit the light field structure. In particular, the moving speed of an object across the views in a light field encodes its depth in the scene, which cannot be captured by a global warping model. Multi-frame algorithms employing more complex warping models exist, for example in video super-resolution [17] [18], yet the warping models do not exactly fit the geometry of light field data and their construction is computationally demanding. In particular, multi-frame video super-resolution involves two main steps, namely optical flow estimation, which finds correspondences between temporally successive frames, and eventually a super-resolution step that is built on the optical flow.

In the light field representation, the views lie on a two-dimensional grid with adjacent views sharing a constant baseline under the assumption of both vertical and horizontal registration. As a consequence, not only would the optical flow computation reduce to disparity estimation, but the disparity map at one view further determines its warping to every other one in the light field, in the absence of occlusions. In [8] Wanner and Goldluecke build over these observations to extract the disparity map at each view directly from the epipolar line slopes with the help of a structure tensor operator. Then, similarly to multi-frame super-resolution, they project all the views to the target one within a global optimization formulation endowed with a *Total Variation* prior. Although the structure tensor operator permits to carry out disparity estimation in the continuos domain, this task remains very challenging at low spatial resolution. As a result, disparity errors unfortunately translate into significant artifacts in the textured areas and along object edges. Finally, each view of the light field has to be processed separately to super-resolve the complete light field, which does not permit to fully exploit the inter-view dependencies.

In another work, Heber and Pock [9] consider the matrix obtained by warping all the views to a reference one, and propose to model it as the sum of a low rank matrix and a noise one, where the later describes the noise and occlusions. This model, that resembles *Robust PCA* [19], is primarily meant for disparity estimation at the reference view. However, the authors show that a slight modification of the objective function can provide a high resolution version of the reference view without further efforts at the optimization stage. It is however important to note that the computed disparity map at the reference view remains at low resolution. The algorithm could finally be applied separately to each view in order to super-resolve the whole light field, but that may not be the ideal solution to that global problem, due to high redundancy in estimating depth maps independently.

In a different framework, Mitra and Veeraraghavan propose a light field super-resolution algorithm based on a learning procedure [10]. Each view in the low resolution light field is divided into patches that are possibly overlapping. Patches at the same spatial position in the different views form a light field with very small spatial resolution, i.e., a light field patch. The authors assume that each light field patch has a constant disparity, i.e., all objects within the light field patch are assumed to lie at the same depth in the scene. Then, super-resolution is carried out separately on the single light field patch. In particular, a *Gaussian Mixture Model* prior for high resolution light field patches is learnt offline for each discrete disparity value and then employed within a *MAP* estimator. Due to the reduced dimensionality of each light field patch, and to the closed form solution of the estimator, this approach requires less online computation than other light field super-resolution algorithms. However, the offline learning strategy has also some drawbacks, and in particular the dependency on the training set, the need for a new learning step for each super-resolution factor, and the disparity discretization process.

Finally, we note that some authors, e.g., Bishop et al. [20], consider the recovery of an all in focus image with full sensor

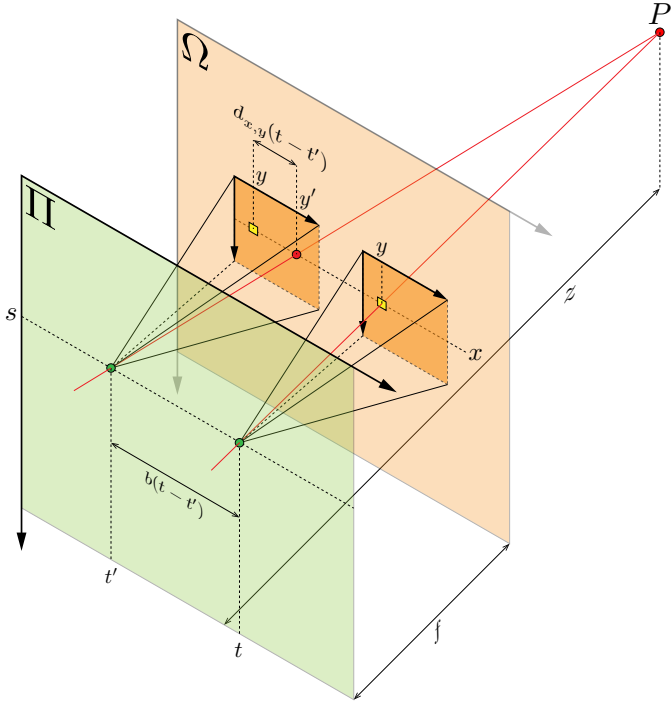


Fig. 1. The two plane parametrization. Two light rays (red lines) are emitted by the same point P in a 3D scene and they intersect the spatial plane Ω and the angular plane Π at different coordinates. The two pyramids represent two pinhole cameras: the camera apertures lie at angular coordinates (s, t') and (s, t) in Π , respectively, and coincide with the pyramid vertices indicated with the two green circles. The angular coordinates have been discretized with a step b , therefore the distance between the two camera apertures is $b(t - t')$. The respective sensors are represented by the two orange squares in the plane Ω and each one has its own spatial reference system. The intersections of the two rays with the sensors of the left and right cameras are indicated with a red dot and a yellow square, respectively. In particular, the yellow square indicates that the point P is projected on the pixel (x, y) of the right camera sensor. The pixel at coordinate (x, y) in the left camera sensor is indicated with a yellow square too. However, in this case, the point P is projected on the spatial coordinate (x, y') , which is indicated with the red circle because it does not necessarily correspond to a pixel, as y' may not be integer. Note that the camera sensors are represented in front of the camera aperture for a matter of consistency, but this does not represent a loss of generality, as the planes Ω and Π can be swapped.

resolution from the light field camera output. They refer to this task as light field super-resolution although it is different from the problem considered in this paper. In this article, no light field applications are considered a priori: the light field views are jointly super-resolved, thus enabling any light field applications to be performed later at a resolution higher than the original one.

III. LIGHT FIELD STRUCTURE

In the light field literature, it is common to parametrize the light rays from a 3D scene by the coordinates of their intersection with two parallel planes, typically referred to as the *spatial plane* Ω and the *angular plane* Π . When we denote the intersection coordinates with $(x, y) \in \Omega$ and $(s, t) \in \Pi$, respectively, the light field function \mathcal{L} maps each ray in the 3D space to its radiance value as follows:

$$\mathcal{L} : \Omega \times \Pi \rightarrow \mathbb{R}, \quad (x, y, s, t) \mapsto \mathcal{L}(x, y, s, t). \quad (1)$$

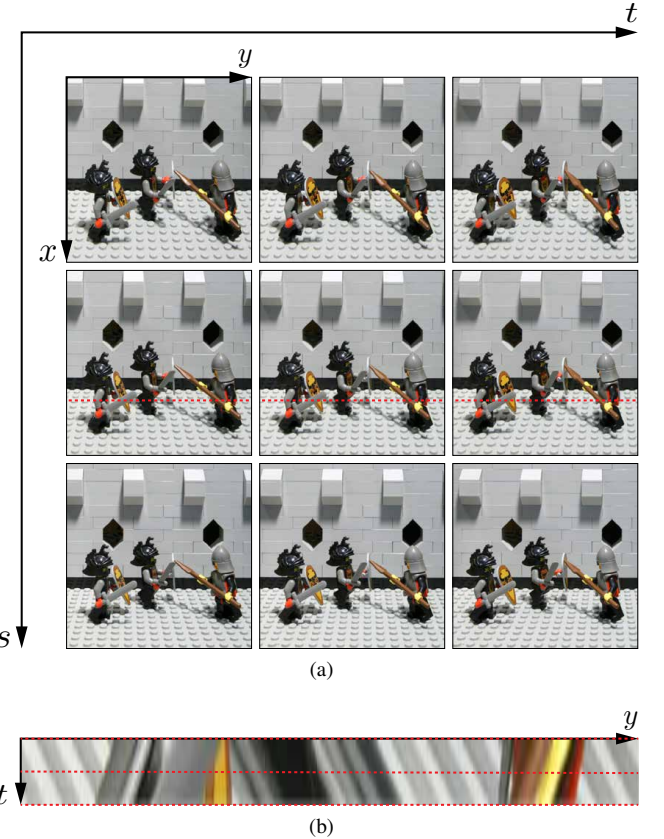


Fig. 2. Example of light field and epipolar image (EPI). Figure (a) shows an array of 3×3 views, obtained from the knights light field (Stanford dataset) which actually consist in an array of 17×17 views. Figure (b) shows an epipolar image from the original 17×17 knights light field. In particular, the t -th row in the epipolar image corresponds to the row $U_{9, t}(730, \cdot)$. The top, central, and bottom red dashed rows in (b) corresponds to the left, central, and right dashed rows in red in the sample views in (a), respectively.

A pinhole camera with its aperture at coordinate $(s, t) \in \Pi$ and its sensor on the spatial plane Ω captures a slice $\mathcal{L}(\cdot, \cdot, s, t) \subseteq \Omega$ of the light field, as its aperture accommodates only those rays crossing Π at (s, t) . This is illustrated in Figure 1. Then, an array of pinhole cameras can provide a regular sampling of the light field in the form of a set of images captured from different points of view. This is the sampling scheme approximated by both camera arrays and light field camera setups.

In more details, we consider the light field as the output of an $M \times M$ array of pinhole cameras, each one equipped with an $N \times N$ pixel sensor. We assume that the apertures and the sensors lie on Π and Ω , respectively. However, differently from (1), we assume that each camera sensor has its own spatial reference system (x, y) in Ω . An example is provided in Figure 2a. The camera apertures perform a sampling of the axes s and t with a step b , while each sensor performs a sampling of its axes x and y with a step equal to the pixel size. With an abuse of notation, we refer to the spatial and angular sampling coordinates as to (x, y) and (s, t) , respectively, with $x, y \in \{1, 2, \dots, N\}$ and $s, t \in \{1, 2, \dots, M\}$. Within this setup, we can represent the light field as an $N \times N \times M \times M$ real matrix \mathbf{U} , with $U(x, y, s, t)$ the intensity of a pixel with coordinates (x, y) in the view (s, t) . In particular, we

denote the view at (s, t) as $\mathbf{U}_{s,t} \equiv \mathbf{U}(\cdot, \cdot, s, t) \in \mathbb{R}^{N \times N}$. Finally, without lack of generality, we assume that each pair of horizontally or vertically adjacent views in the light field are properly registered.

With reference to Figure 1, we now describe in more details the particular structure of the light field data. We consider a point P at depth z from Π , whose projection on one of the cameras is represented by the pixel $\mathbf{U}_{s,t}(x, y)$, in the right view of Figure 1. We now look at the projection of P on the other views $\mathbf{U}_{s,t'}$ in the same row of the camera array, as the left view in Figure 1. We observe that, in the absence of occlusions and under the Lambertian assumption¹, the projection of P obeys the following stereo equation:

$$\begin{aligned} \mathbf{U}_{s,t}(x, y) &= \mathbf{U}_{s,t'}(x, y + (fb/z)(t - t')) \\ &= \mathbf{U}_{s,t'}(x, y') \end{aligned} \quad (2)$$

with f the distance between Ω and Π , b the angular sampling step (i.e., the baseline distance between adjacent cameras). A visual interpretation of Eq. (2) is provided by the *Epipolar Plane Image (EPI)* [21] in Figure 2b, which represents a slice $\mathbf{E}_{x,s} \equiv \mathbf{U}(x, \cdot, s, \cdot) \in \mathbb{R}^{N \times M}$ of the light field. This is obtained by stacking the x -th row from each view $\mathbf{U}_{s,t'}$ on top of each other. It leads to a clear line pattern, as the projection $\mathbf{U}_{s,t}(x, y) \equiv \mathbf{E}_{x,s}(y, t)$ of point P on the view at (s, t) is the pivot of a line hosting all its projections into the other views (s, t') . The line slope depends on the depth of the point in the scene. We stress out that, although $\mathbf{U}_{s,t}(x, y)$ is a pixel in the captured light field, all the other projections $\mathbf{U}_{s,t'}(x, y')$ do not necessarily correspond to actual pixels in the light field images, as y' may not be integer.

We finally observe that Eq. (2) can be extended to the whole light field:

$$\begin{aligned} \mathbf{U}_{s,t}(x, y) &= \mathbf{U}_{s',t'}(x + d_{x,y}(s - s'), y + d_{x,y}(t - t')) \\ &= \mathbf{U}_{s',t'}(x', y') \end{aligned} \quad (3)$$

where $d_{x,y} \equiv \mathbf{D}_{s,t}(x, y) \equiv fb/z$, with $\mathbf{D}_{s,t} \in \mathbb{R}^{N \times N}$ the disparity map of view $\mathbf{U}_{s,t}$ with respect to its left view $\mathbf{U}_{s,t-1}$, as in a standard stereo system. We refer to the model described by Eq. (3) as the *light field structure*.

Later on, for the sake of clarity, we will denote a light field view either by its angular coordinate (s, t) or by its linear coordinate $k = (M(t-1) + s) \in \{1, 2, \dots, M^2\}$. In particular, we have $\mathbf{U}_{s,t} = \mathbf{U}_k$ where \mathbf{U}_k is the k -th view encountered when visiting the camera array in column major order. Finally, we also handle the light field in a vectorized form, with the following notation:

- $\mathbf{u}_{s,t} = \mathbf{u}_k \in \mathbb{R}^{N^2}$ is the vectorized form of view $\mathbf{U}_{s,t}$,
- $\mathbf{u} = [\mathbf{u}_1^\top, \mathbf{u}_2^\top, \dots, \mathbf{u}_{M^2}^\top]^\top \in \mathbb{R}^{N^2 M^2}$,

where the vectorized form of a matrix is simply obtained by visiting its entries in column major order.

IV. PROBLEM FORMULATION

The light field (spatial) super resolution problem concerns the recovery of the high resolution light field \mathbf{U} from its low resolution counterpart \mathbf{V} , at resolution $(N/\alpha) \times (N/\alpha) \times M \times$

¹All the rays emitted by point P exhibit the same radiance.

M with $\alpha \in \mathbb{N}$. Equivalently, we aim at super resolving each view $\mathbf{V}_{s,t} \in \mathbb{R}^{(N/\alpha) \times (N/\alpha)}$ to get its high resolution version $\mathbf{U}_{s,t} \in \mathbb{R}^{N \times N}$. In order to recover the high resolution light field from the low resolution data, we propose to minimize the following objective function:

$$\begin{aligned} \mathbf{u}^* &\in \operatorname{argmin}_{\mathbf{u}} \mathcal{F}(\mathbf{u}) \\ \text{with } \mathcal{F}(\mathbf{u}) &= \mathcal{F}_1(\mathbf{u}) + \lambda_2 \mathcal{F}_2(\mathbf{u}) + \lambda_3 \mathcal{F}_3(\mathbf{u}) \end{aligned} \quad (4)$$

where each term describes one of the constraints about the light field structure and the multipliers λ_2 and λ_3 balance the different terms. We now analyze each one of them separately.

Each pair of high and low resolution views have to be consistent, and we model their relationship as follows:

$$\mathbf{v}_k = \mathbf{S}\mathbf{B}\mathbf{u}_k + \mathbf{n}_k \quad (5)$$

where $\mathbf{B} \in \mathbb{R}^{N^2 \times N^2}$ and $\mathbf{S} \in \mathbb{R}^{(N/\alpha)^2 \times N^2}$ denote a blurring and a sampling matrix, respectively, and the vector $\mathbf{n}_k \in \mathbb{R}^{(N/\alpha)^2}$ captures possible inaccuracies of the assumed model. The first term in Eq. (4) enforces the constraint in Eq. (5) for each high resolution and low resolution view pair, and it is typically referred to as the *data fidelity term*:

$$\mathcal{F}_1(\mathbf{u}) \equiv \sum_k \|\mathbf{S}\mathbf{B}\mathbf{u}_k - \mathbf{v}_k\|_2^2. \quad (6)$$

Then, the various low resolution views in the light field capture the scene from slightly different perspectives; therefore, details dropped by the sampling at one view may survive in another one. Gathering at one view all the complementary information from the others can augment its resolution. This can be achieved by enforcing that the high resolution view \mathbf{u}_k can generate all the other low resolution views $\mathbf{v}_{k'}$ in the light field, with $k' \neq k$. For every view \mathbf{u}_k we thus have the following model:

$$\mathbf{v}_{k'} = \mathbf{S}\mathbf{B}\mathbf{F}_k^{k'} \mathbf{u}_k + \mathbf{n}_k^{k'}, \quad \forall k' \neq k \quad (7)$$

where the matrix $\mathbf{F}_k^{k'} \in \mathbb{R}^{N^2 \times N^2}$ is such that $\mathbf{F}_k^{k'} \mathbf{u}_k \simeq \mathbf{u}_{k'}$; it is typically referred to as a *warping matrix*. The vector $\mathbf{n}_k^{k'}$ captures possible inaccuracies of the model, such as the presence of pixels of $\mathbf{v}_{k'}$ that cannot be generated because they correspond to occluded areas in \mathbf{u}_k . The second term in Eq. (4) enforces the constraint in Eq. (7) for every high resolution view:

$$\mathcal{F}_2(\mathbf{u}) \equiv \sum_k \sum_{k' \in \mathcal{N}_k^+} \|\mathbf{H}_k^{k'} (\mathbf{S}\mathbf{B}\mathbf{F}_k^{k'} \mathbf{u}_k - \mathbf{v}_{k'})\|_2^2 \quad (8)$$

where the matrix $\mathbf{H}_k^{k'} \in \mathbb{R}^{(N/\alpha)^2 \times (N/\alpha)^2}$ is diagonal and binary, and masks those pixels of $\mathbf{v}_{k'}$ that cannot be generated due to occlusions in \mathbf{u}_k , while \mathcal{N}_k^+ denotes a subset of the views (potentially all) with $k \notin \mathcal{N}_k^+$.

Finally, a regularizer \mathcal{F}_3 happens to be necessary in the overall objective function of (4), as the original problem in Eq. (5), and encoded in term \mathcal{F}_1 , is ill-posed due to the fat matrix \mathbf{S} . The second term \mathcal{F}_2 can help, but the warping matrices $\mathbf{F}_k^{k'}$ in Eq. (8) are not known exactly, such that the third term \mathcal{F}_3 is necessary.

We borrow the regularizer from *Graph Signal Processing (GSP)* [22] [23], and define \mathcal{F}_3 as follows:

$$\mathcal{F}_3(\mathbf{u}) \equiv \mathbf{u}^\top \mathbf{L} \mathbf{u} \quad (9)$$

where the positive definite matrix $\mathbf{L} \in \mathbb{R}^{N^2 \times N^2}$ is the *Standard Laplacian* of a graph designed to capture the light field structure. In particular, each pixel in the high resolution light field is modeled as a vertex in a graph, where the edges connect each pixel to its projections on the other views. The quadratic form in Eq. (9) enforces connected pixels to share similar intensity values, thus promoting the light field structure described in Eq. (3).

In particular, we consider an *undirected* weighted graph $\mathcal{G} = (\mathcal{V}, \mathcal{E}, \mathcal{W})$, with \mathcal{V} the set of graph vertices, \mathcal{E} the edge set, and \mathcal{W} a function mapping each edge into a non negative real value, referred to as the edge *weight*:

$$\mathcal{W} : \mathcal{E} \subseteq (\mathcal{V} \times \mathcal{V}) \rightarrow \mathbb{R}, \quad (i, j) \mapsto \mathcal{W}(i, j).$$

The vertex $i \in \mathcal{V}$ corresponds to the entry $\mathbf{u}(i)$ of the high resolution light field. Then, if we denote with $1, 2, \dots, |\mathcal{V}|$ the vertices in \mathcal{V} , with $|\cdot|$ the set cardinality, the graph can be represented through its *adjacency matrix* $\mathbf{W} \in \mathbb{R}^{|\mathcal{V}| \times |\mathcal{V}|}$:

$$\mathbf{W}(i, j) = \begin{cases} \mathcal{W}(i, j) & \text{if } (i, j) \in \mathcal{E} \\ 0 & \text{otherwise.} \end{cases}$$

Since the graph is assumed to be undirected, the adjacency matrix is symmetric: $\mathbf{W}(i, j) = \mathbf{W}(j, i)$. A weight typically captures the similarity between vertices. As a result, we can rewrite the term \mathcal{F}_3 in Eq. (9) as follows:

$$\begin{aligned} \mathcal{F}_3(\mathbf{u}) &\equiv \mathbf{u}^\top \mathbf{L} \mathbf{u} \\ &= \frac{1}{2} \sum_i \sum_{j \sim i} \mathbf{W}(i, j) (\mathbf{u}(i) - \mathbf{u}(j))^2. \end{aligned} \quad (10)$$

The last equality in Eq. (10) shows that the term \mathcal{F}_3 penalizes significant intensity variations along highly weighted edges, therefore its minimization leads to an adaptive smoothing [22], ideally along the EPI lines of Figure 2b in our light field framework.

Differently from the other light field super-resolution methods, the proposed formulation permits to address the recovery of the whole light field altogether, thanks to the global regularizer \mathcal{F}_3 . The term \mathcal{F}_2 permits to augment the resolution of each view without recurring to external data and learning procedures. However, differently from video super-resolution or the light field super-resolution approach in [8], the warping matrices in \mathcal{F}_2 do not rely on a precise estimation of the disparity at each view. This is possible mainly thanks to the graph regularizer \mathcal{F}_3 , that acts on each view as a denoising term based on non local similarities [24] but at the same time jointly constraints the reconstruction of all the views, thus enforcing the full light field structure captured by the graph.

V. SUPER-RESOLUTION ALGORITHM

We now describe the algorithm that we use to solve the optimization problem in Eq. (4). We first discuss the construction of the warping matrices of the term \mathcal{F}_2 in Eq. (8), and then

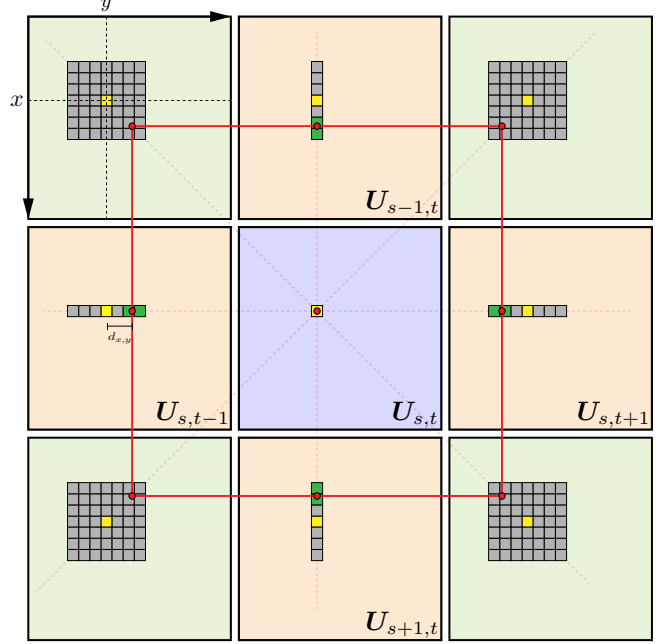


Fig. 3. The neighboring views and the square constraint. All the squares indicate pixels, in particular, all the yellow pixels lie at the spatial coordinates (x, y) in their own view. The projection of pixel $U_{s,t}(x, y)$ on the other eight neighboring views is indicated with a red dot. According to Eq. (3) they all lie on a square, highlighted in red. The four orange views represent the set \mathcal{N}_k^+ , used in the warping matrix construction. In each one of these four views, the two pixels employed in the convex combination targeting pixel $U_{s,t}(x, y)$ are indicated in green and are adjacent to each other. The projection of pixel $U_{s,t}(x, y)$ lies between the two green pixels, and these two belong to a 1D window indicated in gray.

the construction of the graph employed in the regularizer \mathcal{F}_3 in Eq. (9). Finally, we describe the complete super-resolution algorithm.

A. Warping matrix construction

We define the set of the neighboring views \mathcal{N}_k^+ in the term \mathcal{F}_2 in Eq. (8) as containing only the four views $\mathbf{U}_{k'}$ adjacent to \mathbf{U}_k in the light field:

$$\{\mathbf{U}_{k'} : k' \in \mathcal{N}_k^+\} = \{\mathbf{U}_{s,t \pm 1}, \mathbf{U}_{s \pm 1,t}\}.$$

This choice reduces the number of the warping matrices but at the same time does not limit our problem formulation, as the interlaced structure of the term \mathcal{F}_2 constrains together also those pairs of views that are not explicitly constrained in \mathcal{F}_2 .

The inner summation in Eq. (8) considers the set of the four warping matrices $\{\mathbf{F}_k^{k'} : k' \in \mathcal{N}_k^+\}$ that warp the view \mathbf{U}_k to each one of the four views $\mathbf{U}_{k'}$. Conversely, in this section we consider the set of the four warping matrices $\{\mathbf{F}_{k'}^k : k' \in \mathcal{N}_k^+\}$ that warp each one of the four views $\mathbf{U}_{k'}$ to the view \mathbf{U}_k . The warping matrix $\mathbf{F}_{k'}^k$ is such that $\mathbf{F}_{k'}^k \mathbf{u}_{k'} \simeq \mathbf{u}_k$. In particular, the i -th row of the matrix $\mathbf{F}_{k'}^k$ computes the pixel $\mathbf{u}_k(i) = \mathbf{U}_k(x, y) = \mathbf{U}_{s,t}(x, y)$ as a convex combination of those pixels around its projection on $\mathbf{U}_{k'} = \mathbf{U}_{s',t'}$. Note that the convex combination is necessary, as the projection does not lie at integer spatial coordinates in general. The exact position of the projection in $\mathbf{U}_{s',t'}$ is determined by the disparity value $d_{x,y}$ associated to pixel $\mathbf{U}_{s,t}(x, y)$. This is represented in

Figure 3, which shows that the projections of $\mathbf{U}_{s,t}(x, y)$ on the four neighboring views lie on the edges of a virtual square centered on the pixel $\mathbf{U}_{s,t}(x, y)$ and whose size depends on the disparity value $d_{x,y}$. We roughly estimate the disparity value by finding a $\delta \in \mathbb{N}$ such that $d_{x,y} \in [\delta, \delta + 1]$. In details, we first define a similarity score between the target pixel $\mathbf{U}_{s,t}(x, y)$ and a generic pixel $\mathbf{U}_{s',t'}(x', y')$ as follows:

$$w_{s',t'}(x', y') = \exp\left(-\frac{\|\mathcal{P}_{s,t}(x, y) - \mathcal{P}_{s',t'}(x', y')\|_F^2}{\sigma^2}\right) \quad (11)$$

where $\mathcal{P}_{s,t}(x, y)$ denotes a square patch centered at pixel $\mathbf{U}_{s,t}(x, y)$, the operator $\|\cdot\|_F$ denotes the Frobenius norm, and σ is a tunable constant. Then, we center a search window at $\mathbf{U}_{s',t'}(x, y)$ in each one of the four neighboring views, as represented in Figure 3. In particular, we consider

- a $1 \times W$ pixel window for $(s', t') = (s, t \pm 1)$,
- a $W \times 1$ pixel window for $(s', t') = (s \pm 1, t)$,

with $W \in \mathbb{N}$, and odd, defining the disparity range assumed for the whole light field, i.e., $d_{x,y} \in [-\lfloor W/2 \rfloor, \lfloor W/2 \rfloor] \forall (x, y)$. Finally, we introduce the following function that assigns a score to each possible value of δ :

$$\begin{aligned} \mathcal{S}(\delta) = & w_{s,t-1}(x, y + \delta) + w_{s,t-1}(x, y + \delta + 1) \\ & + w_{s,t+1}(x, y - \delta - 1) + w_{s,t+1}(x, y - \delta) \\ & + w_{s-1,t}(x + \delta, y) + w_{s-1,t}(x + \delta + 1, y) \\ & + w_{s+1,t}(x - \delta - 1, y) + w_{s+1,t}(x - \delta, y). \end{aligned} \quad (12)$$

Note that each line of Eq. (12) refers to a pair of adjacent pixels in one of the neighboring views. We finally estimate δ as follows:

$$\delta^* = \underset{\delta \in \{-\lfloor W/2 \rfloor, \dots, \lfloor W/2 \rfloor - 1\}}{\operatorname{argmax}} \mathcal{S}(\delta).$$

We can now fill the i -th row of matrix $\mathbf{F}_{k'}^k$ such that the pixel $\mathbf{u}_k(i) = \mathbf{U}_{s,t}(x, y)$ is computed as the convex combination of the two closest pixels to its projection on $\mathbf{U}_{k'} = \mathbf{U}_{s',t'}$, namely the following two pixels:

$$\begin{aligned} & \{\mathbf{U}_{k'}(x, y + \delta), \mathbf{U}_{k'}(x, y + \delta + 1)\} \text{ for } (s', t') = (s, t - 1), \\ & \{\mathbf{U}_{k'}(x, y - \delta - 1), \mathbf{U}_{k'}(x, y - \delta)\} \text{ for } (s', t') = (s, t + 1), \\ & \{\mathbf{U}_{k'}(x + \delta, y), \mathbf{U}_{k'}(x + \delta + 1, y)\} \text{ for } (s', t') = (s - 1, t), \\ & \{\mathbf{U}_{k'}(x - \delta - 1, y), \mathbf{U}_{k'}(x - \delta, y)\} \text{ for } (s', t') = (s + 1, t), \end{aligned}$$

which are indicated in green in Figure 3. Once the two pixels involved in the convex combination at the i -th row of matrix $\mathbf{F}_{k'}^k$ are determined, the i -th row can be constructed. As an example, let us focus on the left neighboring view $\mathbf{U}_{k'} = \mathbf{U}_{s,t-1}$. The two pixels involved in the convex combination at the i -th row of the matrix $\mathbf{F}_{k'}^k$ are the following:

$$\{\mathbf{u}_{k'}(j_1) = \mathbf{U}_{k'}(x, y + \delta), \mathbf{u}_{k'}(j_2) = \mathbf{U}_{k'}(x, y + \delta + 1)\}.$$

We thus define the i -th row of the matrix $\mathbf{F}_{k'}^k$ as follows:

$$\mathbf{F}_{k'}^k(i, j) = \begin{cases} w_{s,t-1}(x, y + \delta) / w & \text{if } j = j_1 \\ w_{s,t-1}(x, y + \delta + 1) / w & \text{if } j = j_2 \\ 0 & \text{otherwise} \end{cases}$$

with $w = w_{s,t-1}(x, y + \delta) + w_{s,t-1}(x, y + \delta + 1)$. In particular each one of the two pixels in the convex combination

has a weight that is proportional to its similarity to the target pixel $\mathbf{U}_{s,t}(x, y)$. For the remaining three neighboring views we proceed similarly.

We stress out that, for each pixel $\mathbf{u}_k(i) = \mathbf{U}_{s,t}(x, y)$, the outlined procedure fills the i -th row of each one of the four matrices $\mathbf{F}_{k'}^k$ with $k' \in \mathcal{N}_k^+$. In particular, as illustrated in Figure 3, the pair of pixels selected in each one of the four neighboring views encloses one edge of the red square hosting the projections of the pixel $\mathbf{U}_{s,t}(x, y)$, therefore this procedure contributes to enforcing the light field structure in Eq. (3). Later on, we will refer to this particular structure as the *square constraint*.

Finally, since occlusions are mostly handled by the regularizer \mathcal{F}_3 , we use the corresponding diagonal masking matrix $\mathbf{H}_{k'}^k$ in Eq. (8) only to handle the trivial occlusions due to the image borders.

B. Regularization graph construction

The effectiveness of the term \mathcal{F}_3 depends on the graph capability to capture the underlying structure of the light field. Ideally, we would like to connect each pixel $\mathbf{U}_{s,t}(x, y)$ in the light field to its projections on the other views, as these all share the same intensity value under the Lambertian assumption. However, since the projections do not lie at integer spatial coordinates in general, we adopt a procedure similar to the warping matrix construction and we aim at connecting the pixel $\mathbf{U}_{s,t}(x, y)$ to those pixels that are close to its projections on the other views. We thus propose a three step approach to the computation of the adjacency matrix \mathbf{W} of the graph in Eq. (9).

1) *Edge weight computation*: We consider a view $\mathbf{U}_{s,t}$ and define its set of neighboring views \mathcal{N}_k as follows:

$$\mathcal{N}_k \equiv \mathcal{N}_k^+ \cup \mathcal{N}_k^\times$$

where we extend the neighborhood considered in the warping matrix construction with the four diagonal views. In particular, \mathcal{N}_k^\times is defined as follows:

$$\{k' : \mathbf{U}_{k'} \in \mathcal{N}_k^\times\} = \{\mathbf{U}_{s-1,t \pm 1}, \mathbf{U}_{s+1,t \pm 1}\}.$$

The full set of neighboring views is represented in Figure 3, with the views in \mathcal{N}_k^+ in green, and those in \mathcal{N}_k^\times in orange. We now consider a pixel $\mathbf{u}(i) = \mathbf{U}_{s,t}(x, y)$ and define its edges toward one neighboring view $\mathbf{U}_{k'} = \mathbf{U}_{s',t'}$ with $k' \in \mathcal{N}_k$. We center a search window at pixel $\mathbf{U}_{s',t'}(x, y)$ and compute the following similarity score (weight) between pixel $\mathbf{U}_{s,t}(x, y) = \mathbf{u}(i)$ and each pixel $\mathbf{U}_{s',t'}(x', y') = \mathbf{u}(j)$ in the considered window:

$$\mathbf{W}_A(i, j) = \exp\left(-\frac{\|\mathcal{P}_{s,t}(x, y) - \mathcal{P}_{s',t'}(x', y')\|_F^2}{\sigma^2}\right), \quad (13)$$

with the notation already introduced in Section V-A. We repeat the procedure for each one of the eight neighboring views in \mathcal{N}_k , but we employ differently shaped windows at different views:

- a $1 \times W$ pixel window for $(s', t') = (s, t \pm 1)$,
- a $W \times 1$ pixel window for $(s', t') = (s \pm 1, t)$,
- a $W \times W$ pixel window otherwise.

The $W \times W$ pixel window is introduced for the diagonal views $\mathbf{U}_k = \mathbf{U}_{s',t'}$, with $k' \in \mathcal{N}_k^{\times}$, as the projection of the pixel $\mathbf{U}_{s,t}(x,y)$ on these views lies neither along row x , nor along column y . The process is illustrated in Figure 3. Iterating the outlined procedure over each pixel in the light field leads to the construction of the adjacency matrix \mathbf{W}_A . We regard \mathbf{W}_A as the adjacency matrix of a *directed* graph, with the entry $\mathbf{W}_A(i,j)$ storing the weight of the edge from pixel $\mathbf{u}(i)$ to pixel $\mathbf{u}(j)$.

2) *Edge pruning*: We want to keep only the most important connections in the graph. We perform a pruning of the edges leaving pixel $\mathbf{U}_{s,t}(x,y)$ toward the eight neighboring views. We thus keep only

- the two highest weighted edges, for $(s',t') = (s,t \pm 1)$,
- the two highest weighted edges, for $(s',t') = (s \pm 1,t)$,
- the four highest weighted edges, otherwise.

In particular, for the diagonal neighboring views $\mathbf{U}_{k'} = \mathbf{U}_{s',t'}$, with $k' \in \mathcal{N}_k^{\times}$, we allow more flexibility as it is more difficult to detect those pixels that lie close to the projection of $\mathbf{U}_{s,t}(x,y)$. We define \mathbf{W}_B as the adjacency matrix after the pruning.

3) *Symmetric adjacency matrix*: We finally carry out the symmetrization of the matrix \mathbf{W}_B , thus obtaining \mathbf{W} in Eq. (10). We adopt a simple approach for obtaining a symmetric matrix and choose to preserve an edge between two vertexes $\mathbf{u}(i)$ and $\mathbf{u}(j)$ if and only if both entry $\mathbf{W}_B(i,j)$ and $\mathbf{W}_B(j,i)$ are non zero. Note that if this is the case, $\mathbf{W}_B(i,j) = \mathbf{W}_B(j,i)$ necessarily holds true, and the weights are maintained. We conclude by observing that this procedure mimics the well-known *left-right disparity check* of stereo vision [25].

We finally note that the constructed graph can be used to build an alternative warping matrix to the one in Section V-A. We recall that matrix $\mathbf{F}_k^{k'}$ is such that $\mathbf{F}_k^{k'} \mathbf{u}_k \simeq \mathbf{u}_{k'}$, and in particular that the i -th row of the matrix computes the pixel $\mathbf{u}_k(i) = \mathbf{U}_{s,t}(x,y)$ as a convex combination of pixels around its projection on $\mathbf{U}_{k'} = \mathbf{U}_{s',t'}$. We thus observe that the sub-matrix \mathbf{W}_S , obtained by extracting the rows $(k-1)N^2 + 1, \dots, kN^2$ and the columns $(k'-1)N^2, \dots, k'N^2$ from the adjacency matrix \mathbf{W} , represents a directed weighted graph. In this graph, each pixel in view $\mathbf{U}_k = \mathbf{U}_{s,t}$ is connected to a subset of pixels that lie close to its projections on $\mathbf{U}_{k'} = \mathbf{U}_{s',t'}$. We thus normalize the rows of \mathbf{W}_S such that they sum up to one, in order to implement a convex combination, and set $\mathbf{F}_{k'}^k = \mathbf{W}_S$ in Eq. (8) with \mathbf{W}_S the normalized sub-matrix. This alternative approach to the warping matrix construction does however not take the light field structure explicitly into account, but it represents a valid alternative when computational resources are limited, as it directly reuses the regularization graph. We finally observe that the graph construction can be highly parallelized.

C. Optimization algorithm

We now have all the ingredients to solve the optimization problem in (4). We observe that it corresponds to a quadratic

problem. We can first rewrite the first term in Eq. (6) as follows:

$$\begin{aligned}\mathcal{F}_1(\mathbf{u}) &= \|\mathbf{A}\mathbf{u} - \mathbf{v}\|_2^2 \\ &= \mathbf{u}^\top \mathbf{A}^\top \mathbf{A} \mathbf{u} - 2\mathbf{v}^\top \mathbf{A} \mathbf{u} + \mathbf{v}^\top \mathbf{v}\end{aligned}\quad (14)$$

with $\mathbf{A} \equiv \mathbf{I} \otimes \mathbf{S}\mathbf{B}$, $\mathbf{I} \in \mathbb{R}^{M^2}$ the identity matrix, and \otimes the Kronecker product. For the second term in Eq. (8) we introduce the following matrices:

- $\mathbf{H}_k \equiv \text{diag}(\mathbf{H}_k^1, \mathbf{H}_k^2, \dots, \mathbf{H}_k^{M^2})$,
- $\mathbf{F}_k = \mathbf{e}_k^\top \otimes \left[(\mathbf{F}_k^1)^\top (\mathbf{F}_k^2)^\top \dots (\mathbf{F}_k^{M^2})^\top \right]^\top$,

where diag denotes a block diagonal matrix, and $\mathbf{e}_k \in \mathbb{R}^{M^2}$ denotes the k -th vector of the canonical basis, with $\mathbf{e}_k(k) = 1$ and zero elsewhere. We observe that the matrices $\mathbf{H}_k^{k'}$ and $\mathbf{F}_k^{k'}$, originally defined only for $k' \in \mathcal{N}_k^+$, have been extended to the whole light field by assuming them to be zero for $k' \notin \mathcal{N}_k^+$. Finally, it is possible to remove the inner sum in the second term:

$$\begin{aligned}\mathcal{F}_2(\mathbf{u}) &= \sum_k \|\mathbf{H}_k \mathbf{A} \mathbf{F}_k \mathbf{u} - \mathbf{H}_k \mathbf{v}\|_2^2 \\ &= \sum_k \mathbf{u}^\top (\mathbf{H}_k \mathbf{A} \mathbf{F}_k)^\top (\mathbf{H}_k \mathbf{A} \mathbf{F}_k) \mathbf{u} \\ &\quad - 2(\mathbf{H}_k \mathbf{v})^\top (\mathbf{H}_k \mathbf{A} \mathbf{F}_k) \mathbf{u} + (\mathbf{H}_k \mathbf{v})^\top (\mathbf{H}_k \mathbf{v}).\end{aligned}\quad (15)$$

Replacing Eq. (14) and Eq. (15) in Eq. (4) finally permits to rewrite the objective function $\mathcal{F}(\mathbf{u})$ in a quadratic form:

$$\mathbf{u}^* \in \underset{\mathbf{u}}{\text{argmin}} \underbrace{\frac{1}{2} \mathbf{u}^\top \mathbf{P} \mathbf{u} + \mathbf{q}^\top \mathbf{u} + r}_{\mathcal{F}(\mathbf{u})} \quad (16)$$

with

$$\begin{aligned}\mathbf{P} &\equiv 2 \left(\mathbf{A}^\top \mathbf{A} + \lambda_2 \sum_k (\mathbf{H}_k \mathbf{A} \mathbf{F}_k)^\top (\mathbf{H}_k \mathbf{A} \mathbf{F}_k) + \lambda_3 \mathbf{L} \right) \\ \mathbf{q} &\equiv -2 \left(\mathbf{A}^\top + \lambda_2 \sum_k ((\mathbf{H}_k \mathbf{A} \mathbf{F}_k)^\top \mathbf{H}_k) \right) \mathbf{v} \\ r &\equiv \mathbf{v}^\top \left(\mathbf{I} + \lambda_2 \sum_k (\mathbf{H}_k^\top \mathbf{H}_k) \right) \mathbf{v}.\end{aligned}$$

We observe that, in general, the matrix \mathbf{P} is positive semi-definite, therefore it is not possible to solve (16) just by employing the *Conjugate Gradient (CG)* method on the linear system $\nabla \mathcal{F}(\mathbf{u}) = \mathbf{P}\mathbf{u} - \mathbf{q} = 0$. We instead choose to adopt the *Proximal Point (PA)* method, which iteratively solves (16) using the following update rule:

$$\begin{aligned}\mathbf{u}^{(i+1)} &= \text{prox}_{\beta \mathcal{F}}(\mathbf{u}^i) \\ &= \underset{\mathbf{u}}{\text{argmin}} \mathcal{F}(\mathbf{u}) + \frac{1}{2\beta} \|\mathbf{u} - \mathbf{u}^{(i)}\|_2^2 \\ &= \underset{\mathbf{u}}{\text{argmin}} \underbrace{\frac{1}{2} \mathbf{u}^\top \left(\mathbf{P} + \frac{\mathbf{I}}{\beta} \right) \mathbf{u} + \left(\mathbf{q} - \frac{\mathbf{u}^{(i)}}{\beta} \right)^\top \mathbf{u}}_{\mathcal{T}(\mathbf{u})} \\ &= \left(\mathbf{P} + \frac{\mathbf{I}}{\beta} \right)^{-1} \left(\frac{\mathbf{u}^{(i)}}{\beta} - \mathbf{q} \right).\end{aligned}\quad (17)$$

Algorithm 1 Graph-Based Light Field Super-Resolution

Input: $v = [v_1, \dots, v_{M^2}]$, $\alpha \in \mathbb{N}$, $\beta > 0$, $iter$.

Output: $u = [u_1, \dots, u_{M^2}]$.

- 1: $u \leftarrow$ bilinear interp. of v_k by α , $\forall k = 1, \dots, M^2$;
- 2: **for** $i = 1$ **to** $iter$ **do**
- 3: build the graph adjacency matrix W on u ;
- 4: build the matrices F_k on u , $\forall k = 1, \dots, M^2$;
- 5: update the matrix P ;
- 6: update the vector q ;
- 7: $z \leftarrow u$; ▷ Initialize CG
- 8: **while** convergence is reached **do**
- 9: $z \leftarrow \text{CG}(P + (I/\beta), (z/\beta) - q)$;
- 10: **end while**
- 11: $u \leftarrow z$; ▷ Update u
- 12: **end for**
- 13: **return** u ;

The last equality has been obtained by imposing $\nabla \mathcal{T}(u) = 0$. Note that matrix $P + (1/\beta)I$ is positive definite for every $\beta > 0$, hence its inverse is now defined. In practice, however, we do not invert any matrix but use the CG method to solve the linear system $\nabla \mathcal{T}(u) = 0$. The full Graph-Based (GB) super-resolution algorithm is summarized in Algorithm 1. In particular, we observe that both the construction of the warping matrices and of the graph requires the high resolution light field to be available. In order to bypass this causality problem, a fast and rough high resolution estimation of the light field is computed, e.g., via bilinear interpolation, at the bootstrap phase. Then, at each new iteration, the warping matrices and the graph can be re-constructed on the new available estimate of the high resolution light field, and a new estimate can be obtained by solving the problem in (16).

VI. EXPERIMENTS

A. Experimental settings

We now provide extensive experiments, where we analyze the performance of our algorithm and compare it to the competitor algorithms from the recent literature. We tested our algorithm on two public datasets: the *HCI light field dataset* [26] and the *(New) Stanford light field dataset* [27]. The HCI dataset comprises twelve light fields, each one characterized by a 9×9 array of views. Seven light fields have been artificially generated with a 3D creation suite, while the remaining five have been acquired with a traditional SLR camera mounted on a motorized gantry, that permits to move the camera precisely and to emulate a camera array with an arbitrary baseline. The HCI dataset is meant to represent the data from a light field camera, where both the baseline distance b between adjacent views and the disparity range are typically very small. In particular, the disparity range in the HCI dataset is within $[-3, 3]$ pixels. Differently, the Stanford dataset contains light fields whose view baseline and disparity range can be much higher. For this reason, the Stanford dataset does not closely resemble the typical data from a light field camera. However, we include the Stanford dataset in our experiments in order to evaluate the robustness of light field super-resolution methods

to larger disparity ranges, possibly exceeding the assumed one. The Stanford light fields have all been acquired with a gantry, and they are characterized by a 17×17 array of views. In our experiments we crop the test light fields to a 5×5 array of views, i.e., we choose $M = 5$.

In our experiments, we first create the low resolution version of the test light field from the datasets above. The spatial resolution of the test light field U is decreased by a factor $\alpha \in \mathbb{N}$, using Eq. (5) at each channel of each view. In order to match the assumptions of the other frameworks involved in the comparison [8] [10], and without loss of generality, the blur kernel implemented by matrix B is set to an $\alpha \times \alpha$ box filter. The matrix D performs a regular sampling. Then the obtained low resolution light field V is brought back to the original spatial resolution by the super-resolution algorithms under study. This approach guarantees that the final spatial resolution of the test light field is exactly its original one, regardless of α .

In our framework, the low resolution light field V is divided into possibly overlapping sub-light-fields and each one is reconstructed separately. Formally, a sub-light-field is obtained by fixing a spatial coordinate (x, y) and then extracting an $N' \times N'$ patch with the top left pixel at (x, y) from each view $V_{s,t}$. The result is an $N' \times N' \times M \times M$ light field, with $N' < (N/\alpha)$. Once all the sub-light-fields are super resolved, different estimates of the same pixel produced by the possible overlap are simply averaged. We set $N' = 100$ and 70 for $\alpha = 2$ and 3, respectively. This choice leads to a high resolution sub-light-field with a spatial resolution that is approximatively 200×200 . Finally, only the luminance channel of the low resolution light field is super resolved using our method, as the two chrominance channels can be easily up-sampled via bilinear (or bicubic) interpolation due to their low frequency nature.

In our experiments we consider two variants of our Graph-Based super-resolution algorithm (GB). The first is *GB-SQ*, the main variant, which employs the warping matrix construction based on the square constraint (SQ) and is presented in Section V-A. The second is *GB-DR*, the variant employing the warping matrices extracted directly (DR) from the graph and introduced at the end of Section V-B. In the warping matrix construction in Eq. (11), as well as in the graph construction in Eq. (13), we empirically set the size of patch P to 7×7 pixels, and $\sigma = 0.7229$. For the search window size, we set $W = 13$ pixels. This choice is equivalent to considering a disparity range of $[-6, 6]$ pixels at high resolution. Note that this range happens to be loose for the HCI dataset, whose disparity range is within $[-3, 3]$. Choosing exactly the correct disparity range for each light field could both improve the reconstruction by avoiding wrong correspondences in the graph and warping matrices, and decrease the computation time. On the other hand, for some light fields in the Stanford dataset, the chosen disparity range may become too small, thus preventing the possibility to capture the correct correspondences. In practice, the disparity range is not always available, hence the value $[-6, 6]$ happens to be a fair choice considering that our super-resolution framework targets data from light field cameras, i.e., data with a typically small disparity range. Finally, we

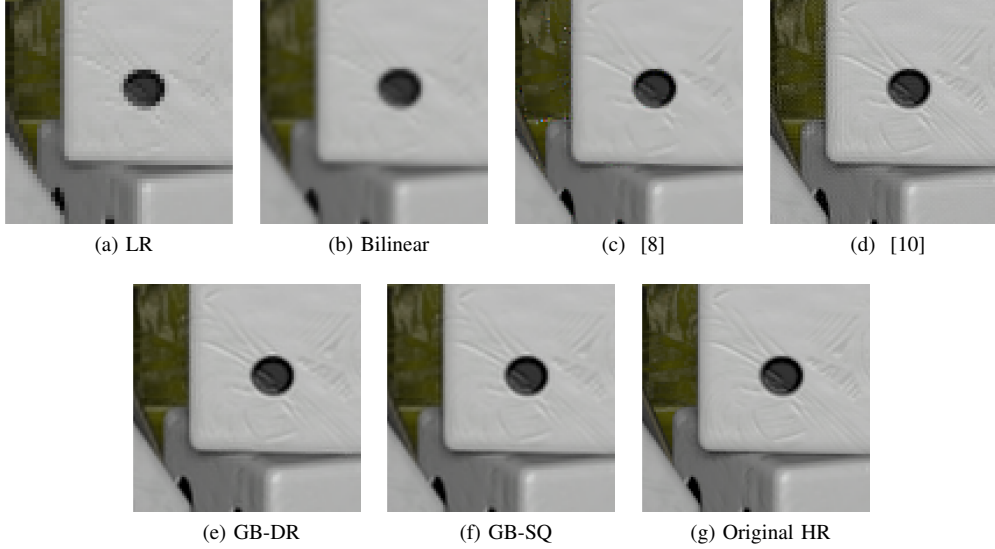


Fig. 4. Detail from the bottom right view of the light field buddha, in the HCI dataset. The low resolution light field in (a) is super-resolved by a factor $\alpha = 2$ with bilinear interpolation in (b), the method [8] in (c), the method [10] in (d), GB-DR in (e) and GB-SQ in (f). The original high resolution light field is provided in (g).

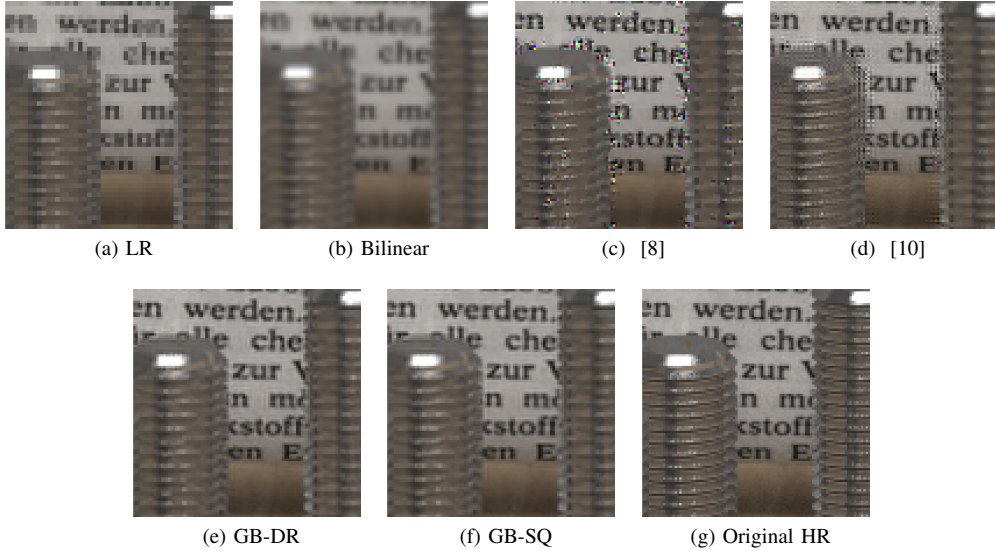


Fig. 5. Detail from the bottom right view of the light field horses, in the HCI dataset. The low resolution light field in (a) is super-resolved by a factor $\alpha = 2$ with bilinear interpolation in (b), the method [8] in (c), the method [10] in (d), GB-DR in (e) and GB-SQ in (f). The original high resolution light field is provided in (g).

empirically set $\lambda_2 = 0.2$ and $\lambda_3 = 0.0055$ in the objective function in Eq. (4) and perform just two iterations of the full Algorithm 1, as we experimentally found them to be enough.

We compare GB with two of the state-of-the-art light field super-resolution methods introduced in Section II: Wanner and Goldluecke [8], and Mitra and Veeraraghavan [10]. We carry out our experiments on the light field super resolution algorithms in [8] using the original code by the authors, available online within the last release of the image processing library *cocolib*. For a fair comparison, we provide the $[-6, 6]$ pixel range at the library input, in order to permit the removal of outliers in the estimated disparity maps. For our experiments on the algorithm in [10] we use the code provided by the

authors. We discretize the $[-6, 6]$ pixel range using a 0.2 pixel step, and for each disparity value we train a different GMM prior for $4 \times 4 \times M \times M$ light field patches. A light field patch is equivalent to a sub-light-field, but with a very small spatial resolution. We perform the training on the data that comes together with the authors' code. Finally, as a baseline reconstruction, we consider also the high resolution light field obtained from bilinear interpolation of the single low resolution views.

In the experiments, our super-resolution method GB, the method in [10], and the bilinear interpolation one, super-resolve only the light field luminance. The full color high resolution light field is obtained through bilinear interpolation

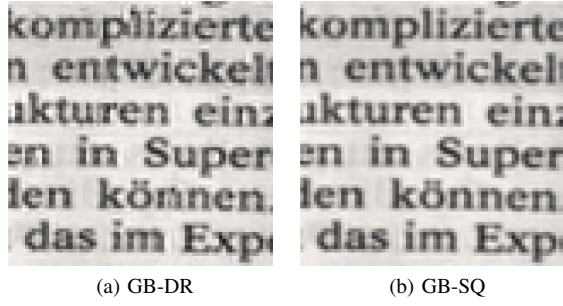


Fig. 6. Detail from the central view of the super-resolved light field *horses*, in the HCI dataset, for the super-resolution factor $\alpha = 2$. The reconstruction provided by GB-SQ (right) exhibits sharper letters than the reconstruction by GB-DR (left), as the square constraint captures better the light field structure.

of the two low resolution light field chrominances. Instead, for the method in [8], the corresponding *cocolib* library needs to be fed with the full color low resolution light field and a full color high resolution light field is provided at the output.

B. Light fields reconstruction results

The numerical results from our super-resolution experiments on the HCI and Stanford datasets are reported in Tables I and II for a super-resolution factor $\alpha = 2$ and respectively for $\alpha = 3$ in Tables III and IV. For each reconstructed light field we compute the PSNR (dB) at each view and report the average and variance of the computed PSNRs in the tables. The PSNRs are computed on the luminance of the light field views². Finally, for a fair comparison with the method in [10], which suffers from border effects, a 15-pixel border has been removed from all the reconstructed views before PSNR computation.

For a super-resolution factor $\alpha = 2$ in the HCI dataset, GB provides the highest average PSNR on ten out of twelve light fields. In particular, nine out of ten of the highest average PSNRs are due to GB-SQ. The highest average PSNR in the two remaining light fields *buddha* and *horses* is achieved by [10], but the corresponding variances are non negligible. The large variance generally indicates that the quality of the central views is larger than the one of the lateral views. This is clearly non ideal, as our objective is to reconstruct all the views with high quality, as necessary in most light field applications. We note however that GB provides a better visual quality in these two light fields. This is shown in Figure 4 and 5, where two details from the bottom right views of the light fields *buddha* and *horses*, respectively, are given for each method. In particular, the reconstruction provided by [10] exhibits strong artifacts along object boundaries. This method assumes a constant disparity within each light field patch that it processes, but patches capturing object boundaries are characterized by an abrupt change of disparity that violates this assumption and causes unpleasant artifacts. Figures 4 and 5 show that also the reconstructions provided by the method in [8] exhibit strong artifacts along edges, although

the disparity is estimated at each pixel in this case. This is due to the presence of errors in the estimated disparity at object boundaries. These errors are caused both by the poor performance of the tensor structure operator in the presence of occlusions, and more in general to the challenges posed by disparity estimation at low resolution. We also observe that the TV term in [8] tends to over-smooth the fine details, as evident in the dice of Figure 4. The bilinear interpolation method provides the lowest PSNR values and the poor quality of its reconstructions is confirmed by the Figures 4 and 5, which appear significantly blurred. In particular, the fine structure around the black spot in the dice of Figure 4 is almost absent in the reconstruction provided by the bilinear interpolation method, and some letters in Figure 5 cannot be discerned. Finally, the numerical results suggest that our GB-SQ methods is more effective in capturing the correct correspondences between adjacent views in the light field. A visual example is provided in Figure 6, where the letters in the view reconstructed by GB-SQ are sharper than those in the view reconstructed by GB-DR.

For the same super-resolution factor $\alpha = 2$ in the Stanford dataset, our graph-based algorithms provide the highest PSNR for all the light fields, while the algorithms in [8] and [10] perform even worse than bilinear interpolation on most of the cases. This very poor performance of [10] is caused by the disparity range characterizing the Stanford dataset, which happens to exceed the $[-6, 6]$ pixel range that is actually considered in our experiments. As a consequence, objects with a disparity exceeding the disparity range may not be super-resolved properly. This phenomenon is exemplified in Figure 7, where a vertical stripe from the central view of the light field *bracelet* is shown. The three details in the bottom, middle, and top part of the image lie at increasing depths in the scene, therefore they have decreasing associated disparities. As expected, the reconstruction provided by [10] improves from the bottom toward the top of the image, as the disparity range becomes narrower, and finally fits the assumed disparity range. The method in [8] instead fails in both the areas, and in general on the whole Stanford light field, as the structure tensor operator cannot detect large disparity values [28]. Finally, in Table II we also observe that GB-DR happens to be more robust than GB-SQ when the disparity range assumption is not fulfilled. An extreme example is again provided by the *bracelet* light field, where GB-DR provides the highest average PSNR, while GB-SQ performs worse than bilinear interpolation. In particular, we see in Figure 7 that GB-DR successfully reconstructs all the three details despite their different disparity ranges, while GB-SQ introduces artifacts especially in the bottom detail. The artifacts are mostly caused by the wrong constraints imposed by the warping matrices inside term \mathcal{F}_2 of our objective function. These constraints are stronger in GB-SQ than in GB-DR, hence the artifacts are more visible.

We now consider a larger super-resolution factor of $\alpha = 3$. In the HCI dataset, the method in [10] provides the highest average PSNRs on half of the light fields, while GB provides the highest PSNRs only on five (see Table III). However, the average PSNR happens to be a very misleading index here.

² The *cocolib* library, which implements the method in [8], does not provide the light field luminance, therefore this is computed from the high resolution color light field at the library output.

TABLE I
HCI DATASET - PSNR MEAN AND VARIANCE FOR $\alpha = 2$

	Bilinear	[8]	[10]	GB-DR	GB-SQ
buddha	35.22 \pm 0.00	38.22 \pm 0.11	39.12 \pm 0.62	38.53 \pm 0.07	38.96 \pm 0.14
buddha2	30.97 \pm 0.00	33.01 \pm 0.11	33.63 \pm 0.22	34.13 \pm 0.01	34.38 \pm 0.02
couple	25.52 \pm 0.00	26.22 \pm 1.61	31.83 \pm 2.80	32.51 \pm 0.17	33.40 \pm 0.26
cube	26.06 \pm 0.00	26.40 \pm 1.90	30.99 \pm 3.02	32.37 \pm 0.23	33.19 \pm 0.34
horses	26.37 \pm 0.00	29.14 \pm 0.63	33.13 \pm 0.72	30.97 \pm 0.06	32.58 \pm 0.14
maria	32.84 \pm 0.00	35.60 \pm 0.33	37.03 \pm 0.44	37.11 \pm 0.03	37.20 \pm 0.02
medieval	30.07 \pm 0.00	30.53 \pm 0.67	33.34 \pm 0.71	33.18 \pm 0.03	33.41 \pm 0.02
mona	35.11 \pm 0.00	37.54 \pm 0.64	38.32 \pm 1.14	39.23 \pm 0.03	39.31 \pm 0.04
papillon	36.19 \pm 0.00	39.91 \pm 0.15	40.59 \pm 0.89	40.84 \pm 0.06	40.62 \pm 0.04
pyramide	26.49 \pm 0.00	26.73 \pm 1.42	33.35 \pm 4.06	34.28 \pm 0.33	35.30 \pm 0.65
statue	26.32 \pm 0.00	26.15 \pm 2.15	32.95 \pm 4.67	34.40 \pm 0.37	35.46 \pm 0.70
stillLife	25.28 \pm 0.00	25.58 \pm 1.41	28.84 \pm 0.82	30.70 \pm 0.07	30.92 \pm 0.05

TABLE II
STANFORD DATASET - PSNR MEAN AND VARIANCE FOR $\alpha = 2$

	Bilinear	[8]	[10]	GB-DR	GB-SQ
amethyst	35.59 \pm 0.01	24.18 \pm 0.20	36.08 \pm 4.12	40.16 \pm 0.10	39.13 \pm 0.24
beans	47.92 \pm 0.01	23.28 \pm 0.53	36.02 \pm 7.38	49.73 \pm 0.13	48.27 \pm 1.11
bracelet	33.02 \pm 0.00	18.98 \pm 0.22	19.91 \pm 3.86	38.58 \pm 0.38	28.10 \pm 2.23
bulldozer	34.94 \pm 0.01	22.82 \pm 0.09	32.05 \pm 3.73	36.92 \pm 0.28	35.66 \pm 0.36
bunny	42.44 \pm 0.01	26.22 \pm 1.15	40.66 \pm 6.69	46.96 \pm 0.05	46.88 \pm 0.06
cards	29.50 \pm 0.00	19.38 \pm 0.22	28.46 \pm 5.68	36.06 \pm 0.22	36.32 \pm 0.25
chess	36.36 \pm 0.00	21.77 \pm 0.27	34.74 \pm 5.85	41.57 \pm 0.06	41.62 \pm 0.08
eucalyptus	34.09 \pm 0.00	25.04 \pm 0.28	34.90 \pm 3.50	38.80 \pm 0.12	38.96 \pm 0.08
knights	34.31 \pm 0.04	21.14 \pm 0.24	29.33 \pm 4.77	38.95 \pm 0.27	36.98 \pm 0.43
treasure	30.83 \pm 0.00	22.81 \pm 0.15	30.52 \pm 2.93	36.85 \pm 0.21	37.18 \pm 0.17
truck	36.26 \pm 0.04	25.77 \pm 0.08	37.52 \pm 4.60	40.88 \pm 0.14	41.41 \pm 0.17

TABLE III
HCI DATASET - PSNR MEAN AND VARIANCE FOR $\alpha = 3$

	Bilinear	[8]	[10]	GB-DR	GB-SQ
buddha	32.58 \pm 0.01	34.92 \pm 0.63	35.36 \pm 0.34	35.39 \pm 0.02	35.36 \pm 0.02
buddha2	28.14 \pm 0.00	29.96 \pm 0.07	30.29 \pm 0.10	30.49 \pm 0.00	30.41 \pm 0.00
couple	22.62 \pm 0.00	23.02 \pm 1.56	27.43 \pm 1.16	26.60 \pm 0.01	26.90 \pm 0.00
cube	23.25 \pm 0.00	22.47 \pm 2.65	26.48 \pm 1.16	27.17 \pm 0.01	27.34 \pm 0.01
horses	24.35 \pm 0.00	24.45 \pm 1.27	29.90 \pm 0.55	25.52 \pm 0.00	26.39 \pm 0.01
maria	30.02 \pm 0.00	30.64 \pm 0.87	33.36 \pm 0.37	33.44 \pm 0.01	33.08 \pm 0.01
medieval	28.29 \pm 0.00	28.54 \pm 0.37	29.78 \pm 0.50	29.22 \pm 0.00	29.52 \pm 0.01
mona	32.05 \pm 0.00	33.42 \pm 0.52	33.31 \pm 0.40	34.63 \pm 0.01	34.44 \pm 0.01
papillon	33.66 \pm 0.00	36.76 \pm 0.13	36.13 \pm 0.48	36.39 \pm 0.01	36.14 \pm 0.01
pyramide	23.39 \pm 0.00	23.60 \pm 2.72	29.13 \pm 1.86	28.27 \pm 0.02	28.41 \pm 0.01
statue	23.21 \pm 0.00	22.97 \pm 3.63	28.93 \pm 2.03	28.13 \pm 0.02	28.31 \pm 0.01
stillLife	23.28 \pm 0.00	23.62 \pm 1.64	27.23 \pm 0.49	24.96 \pm 0.00	25.50 \pm 0.00

TABLE IV
STANFORD DATASET - PSNR MEAN AND VARIANCE FOR $\alpha = 3$

	Bilinear	[8]	[10]	GB-DR	GB-SQ
amethyst	32.69 \pm 0.01	21.94 \pm 0.30	31.47 \pm 1.07	35.90 \pm 0.03	35.58 \pm 0.02
beans	43.81 \pm 0.01	22.66 \pm 0.26	31.25 \pm 1.85	48.46 \pm 0.10	47.17 \pm 0.40
bracelet	29.06 \pm 0.00	17.37 \pm 0.22	15.83 \pm 0.32	35.03 \pm 0.06	30.36 \pm 0.89
bulldozer	31.88 \pm 0.00	21.85 \pm 0.11	26.21 \pm 0.85	35.31 \pm 0.05	35.17 \pm 0.04
bunny	39.03 \pm 0.00	23.40 \pm 1.22	35.88 \pm 1.82	43.65 \pm 0.05	43.46 \pm 0.05
cards	26.13 \pm 0.00	17.77 \pm 0.33	25.22 \pm 1.40	30.94 \pm 0.02	31.41 \pm 0.03
chess	33.11 \pm 0.00	20.56 \pm 0.24	31.19 \pm 1.96	36.79 \pm 0.04	36.70 \pm 0.03
eucalyptus	31.71 \pm 0.00	23.38 \pm 0.17	32.23 \pm 1.61	34.45 \pm 0.01	34.73 \pm 0.01
knights	31.31 \pm 0.02	19.36 \pm 0.07	25.55 \pm 1.40	35.29 \pm 0.06	35.12 \pm 0.05
treasure	27.98 \pm 0.00	21.45 \pm 0.14	27.86 \pm 0.89	31.27 \pm 0.01	31.14 \pm 0.01
truck	33.52 \pm 0.02	23.27 \pm 0.05	33.04 \pm 1.66	36.60 \pm 0.05	36.89 \pm 0.05

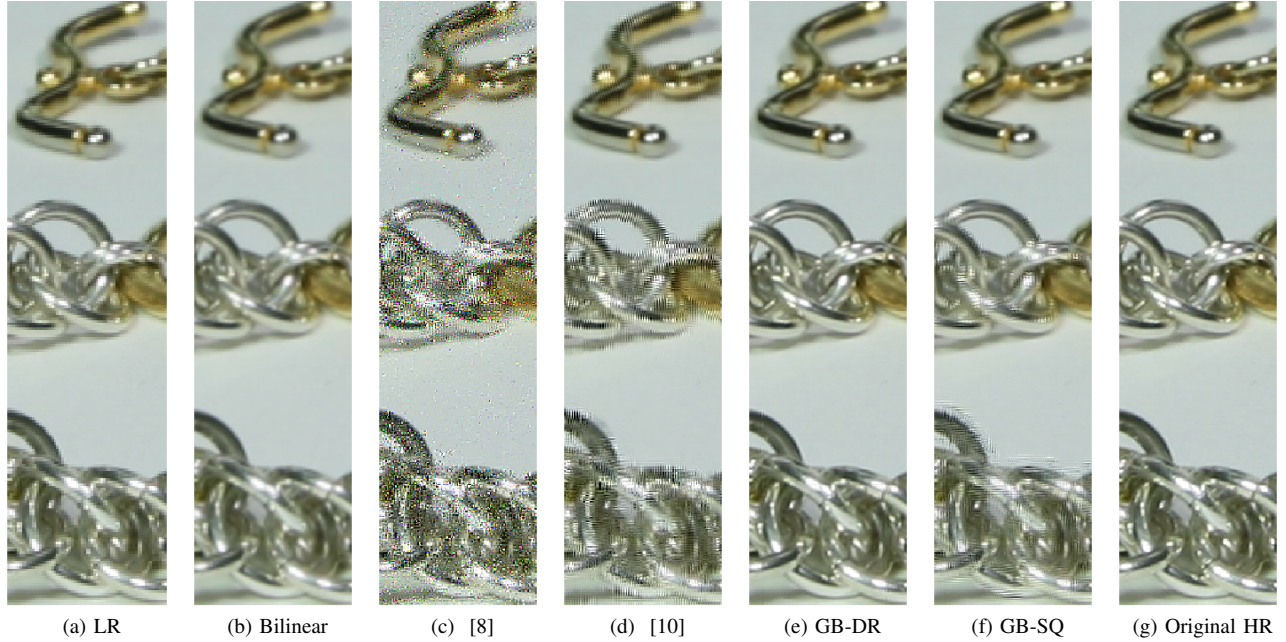


Fig. 7. Detail from the central view of the light field bracelet, in the Stanford dataset. The low resolution light field in (a) is super-resolved by a factor $\alpha = 2$ with bilinear interpolation in (b), the method [8] in (c), the method [10] in (d), GB-DR in (e) and GB-SQ in (f). The original high resolution light field is provided in (g).

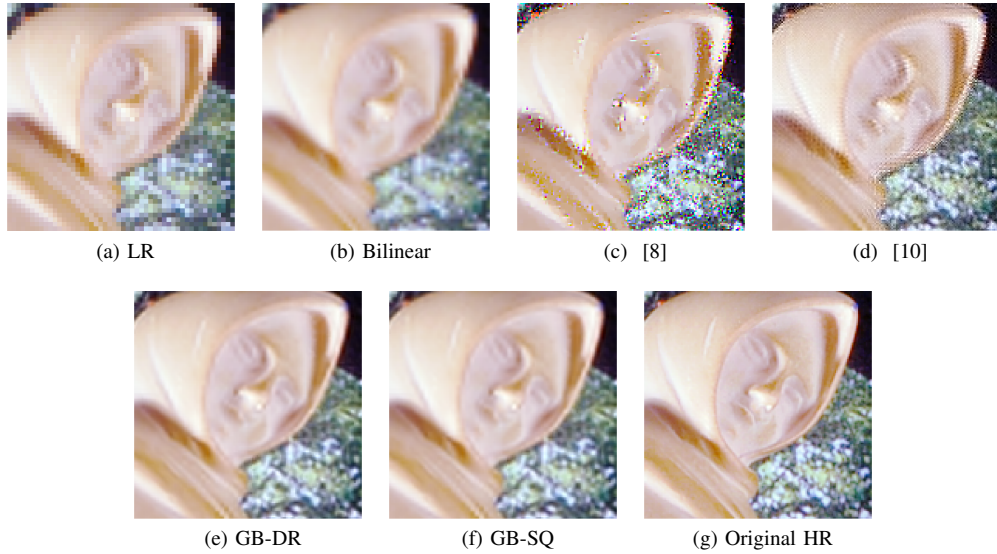


Fig. 8. Detail from the central view of the light field statue, in the HCI dataset. The low resolution light field in (a) is super-resolved by a factor $\alpha = 3$ with bilinear interpolation in (b), the method [8] in (c), the method [10] in (d), GB-DR in (e) and GB-SQ in (f). The original high resolution light field is provided in (g).

In particular, the method in [10] provides the highest average PSNR on the light field statue, but the PSNR variance is larger than 2 dB, which indicates a very large difference in the quality of the reconstructed images. On the other hand, GB-SQ provides a slightly lower average PSNR on the same light field, but the PSNR variance is 0.17 dB, which suggests a more homogenous quality of the reconstructed light field views. In particular, the lowest PSNR provided by GB-SQ among all the views is equal to 28.12 dB, which is significantly higher than the worst case view reconstructed by [10]. Moreover, the

light fields reconstructed by [10] exhibit very strong artifacts along object boundaries. An example is provided in Figure 8, which represents a detail from the central view of the light field statue. The head of the statue reconstructed by [10] happens to be very noisy, especially at the depth discontinuity between the head and the background, while GB is not significantly affected. The lower average PSNRs provided by GB on some light field, when compared to [10], is caused by the very poor resolution of the input data for $\alpha = 3$, that makes the capture of the correct matches for the warping

matrix construction more and more challenging. However, as suggested by Figure 8, the regularizer \mathcal{F}_3 manages to compensate for these errors. The method in [8] performs worse than [10] and GB both in terms of PSNR and visually. As an example, in Figure 8 the reconstruction provided by [8] shows strong artifacts not only at depth discontinuities, but especially in the background, which consists of a flat panel with a tree motive. Despite the very textured background, the tensor structure fails to capture the correct depth due to the very low resolution of the views, and this has a dramatic impact on the final reconstruction. In general, depth estimation at very low resolution happens to be a very challenging task. Finally, the worst numerical results are provided mainly by the bilinear interpolation method, which does not exhibit strong artifacts in general, but provides very blurred images, as shown in Figure 8 and expected.

Finally, for the Stanford dataset, the numerical results in Table IV show the same behavior already observed for $\alpha = 2$. The methods [8] and [10] do not manage to achieve an effective reconstruction due to the disparity range exceeding the assumed one. Instead, GB-SQ and GB-DR manage to adapt reasonably well, as they are less sensitive to the improper choice of the disparity range.

Our experiments show that the proposed super-resolution algorithm GB has some remarkable reconstruction properties that make it preferable over its considered competitors. First, its reconstructed light fields exhibit a better visual quality, often confirmed numerically by the PSNR measure. In particular, GB leads to sharp edges while avoiding the unpleasant artifacts due to depth discontinuities. Second, it provides a uniform reconstruction of all the views in the light field, which is a fundamental requirement for light field applications. Third, it is more robust than the other considered methods in those scenarios where some objects in the scene exceed the assumed disparity range, as it may be the case in practice, where there is no control on the scene.

VII. CONCLUSIONS

We developed a new light field super-resolution algorithm that exploits the complementary information encoded in the different views to augment their spatial resolution, and that relies on a graph to regularize the target light field. We showed how to construct the warping matrices necessary to broadcast the complementary information in each view to the whole light field. In particular, we showed that coupling an approximate warping matrix construction strategy with a graph regularizer that enforces the light field structure can avoid to carry out an explicit, and costly, disparity estimation step on each view. We also showed how to extract the warping matrices directly from the graph when computation needs to be kept at the minimum. Finally, we showed that the proposed algorithm reduces to a simple quadratic formulation, that can be solved efficiently with standard convex optimization tools.

The proposed algorithm compares favorably to the recent state-of-the art methods for light field super resolution, both in terms of PSNR and visual quality. Moreover, the proposed algorithm provides a uniform reconstruction of all the views

in the light field, which is a property that is not present in the other methods. Finally, although the proposed framework is meant mainly for light field camera data, where the disparity range is typically small, it happens to be flexible enough to handle light fields with larger disparity ranges too.

ACKNOWLEDGEMENTS

We express our thanks to the Fonds National Suisse, which supported this work within the project NURIS, and also to Prof. Christine Guillemot (INRIA Rennes) for the valuable discussions.

REFERENCES

- [1] M. Levoy and P. Hanrahan, “Light field rendering,” in *Proceedings of the 23rd ACM annual conference on Computer graphics and interactive techniques*, 1996, pp. 31–42.
- [2] S. J. Gortler, R. Grzeszczuk, R. Szeliski, and M. F. Cohen, “The lumigraph,” in *Proceedings of the 23rd ACM annual conference on Computer graphics and interactive techniques*, 1996, pp. 43–54.
- [3] B. Wilburn, N. Joshi, V. Vaish, E.-V. Talvala, E. Antunez, A. Barth, A. Adams, M. Horowitz, and M. Levoy, “High performance imaging using large camera arrays,” in *ACM Transactions on Graphics (TOG)*, vol. 24, 2005, pp. 765–776.
- [4] “Lytro Inc,” <https://www.lytro.com/>.
- [5] “Ratrix GmbH,” <https://www.raytrix.de/>.
- [6] R. Ng, M. Levoy, M. Brédif, G. Duval, M. Horowitz, and P. Hanrahan, “Light field photography with a hand-held plenoptic camera,” *Computer Science Technical Report CSTR*, vol. 2, no. 11, pp. 1–11, 2005.
- [7] C. Perwass and L. Wietzke, “Single lens 3d-camera with extended depth-of-field,” in *Proceedings of the IS&T/SPIE Electronic Imaging conference*, 2012, pp. 829 108–829 108.
- [8] S. Wanner and B. Goldluecke, “Variational light field analysis for disparity estimation and super-resolution,” *IEEE Transactions on Pattern Analysis and Machine Intelligence*, vol. 36, no. 3, pp. 606–619, 2014.
- [9] S. Heber and T. Pock, “Shape from light field meets robust PCA,” in *Proceedings of the European Conference on Computer Vision*. Springer, 2014, pp. 751–767.
- [10] K. Mitra and A. Veeraraghavan, “Light field denoising, light field superresolution and stereo camera based refocussing using a GMM light field patch prior,” in *Proceedings of the IEEE Conference on Computer Vision and Pattern Recognition Workshops*, 2012, pp. 22–28.
- [11] Jianchao Yang, J. Wright, T. S. Huang, and Yi Ma, “Image Super-Resolution Via Sparse Representation,” *IEEE Transactions on Image Processing*, vol. 19, no. 11, pp. 2861–2873, Nov. 2010.
- [12] Xinbo Gao, Kaibing Zhang, Dacheng Tao, and Xuelong Li, “Joint Learning for Single-Image Super-Resolution via a Coupled Constraint,” *IEEE Transactions on Image Processing*, vol. 21, no. 2, pp. 469–480, Feb. 2012.
- [13] D. Glasner, S. Bagon, and M. Irani, “Super-resolution from a single image,” in *Proceedings of the IEEE 12th International Conference on Computer Vision*, 2009, pp. 349–356.
- [14] M. Bevilacqua, A. Roumy, C. Guillemot, and M.-L. Alberi Morel, “Single-Image Super-Resolution via Linear Mapping of Interpolated Self-Examples,” *IEEE Transactions on Image Processing*, vol. 23, no. 12, pp. 5334–5347, Dec. 2014.
- [15] M. Irani and S. Peleg, “Improving resolution by image registration,” *CVGIP: Graph. Models Image Process.*, vol. 53, no. 3, pp. 231–239, Apr. 1991.
- [16] S. Farsiu, M. Robinson, M. Elad, and P. Milanfar, “Fast and Robust Multiframe Super Resolution,” *IEEE Transactions on Image Processing*, vol. 13, no. 10, pp. 1327–1344, Oct. 2004.
- [17] D. Mitzel, T. Pock, T. Schoenemann, and D. Cremers, “Video super resolution using duality based tv- ℓ_1 optical flow,” in *Proceedings of the Joint Pattern Recognition Symposium*, 2009, pp. 432–441.
- [18] M. Unger, T. Pock, M. Werlberger, and H. Bischof, “A convex approach for variational super-resolution,” in *Proceedings of the Joint Pattern Recognition Symposium*, 2010, pp. 313–322.
- [19] E. J. Candès, X. Li, Y. Ma, and J. Wright, “Robust principal component analysis?” *Journal of the ACM*, vol. 58, no. 3, pp. 1–37, May 2011.

- [20] T. E. Bishop and P. Favaro, "The Light Field Camera: Extended Depth of Field, Aliasing, and Superresolution," *IEEE Transactions on Pattern Analysis and Machine Intelligence*, vol. 34, no. 5, pp. 972–986, May 2012.
- [21] R. C. Bolles, H. H. Baker, and D. H. Marimont, "Epipolar-plane image analysis: An approach to determining structure from motion," *International Journal of Computer Vision*, vol. 1, no. 1, pp. 7–55, 1987.
- [22] A. Elmoataz, O. Lezoray, and S. Bougleux, "Nonlocal discrete regularization on weighted graphs: a framework for image and manifold processing," *IEEE Transactions on Image Processing*, vol. 17, no. 7, pp. 1047–1060, 2008.
- [23] D. I. Shuman, S. K. Narang, P. Frossard, A. Ortega, and P. Vandergheynst, "The emerging field of signal processing on graphs: Extending high-dimensional data analysis to networks and other irregular domains," *IEEE Signal Processing Magazine*, vol. 30, no. 3, pp. 83–98, May 2013.
- [24] A. Kheradmand and P. Milanfar, "A General Framework for Regularized, Similarity-Based Image Restoration," *IEEE Transactions on Image Processing*, vol. 23, no. 12, pp. 5136–5151, Dec. 2014.
- [25] P. Fua, "A parallel stereo algorithm that produces dense depth maps and preserves image features," *Machine vision and applications*, vol. 6, no. 1, pp. 35–49, 1993.
- [26] S. Wanner, S. Meister, and B. Goldluecke, "Datasets and Benchmarks for Densely Sampled 4d Light Fields." in *Proceedings of the VMV*, 2013, pp. 225–226.
- [27] "The (New) Stanford Light Field Archive," <http://lightfield.stanford.edu/>.
- [28] M. Diebold and B. Goldluecke, "Epipolar plane image refocusing for improved depth estimation and occlusion handling," in *Proceedings of the VMV*, 2013.